



HAL
open science

A study of the hadronic resonance structure in the decay $\tau \rightarrow 3\pi\nu_{\tau}$

P. Abreu, W. Adam, T. Adye, P. Adzic, G D. Alekseev, R. Alemany, P P.
Allport, S. Almeded, U. Amaldi, S. Amato, et al.

► **To cite this version:**

P. Abreu, W. Adam, T. Adye, P. Adzic, G D. Alekseev, et al.. A study of the hadronic resonance structure in the decay $\tau \rightarrow 3\pi\nu_{\tau}$. Physics Letters B, 1998, 426, pp.411-427. 10.1016/S0370-2693(98)00347-5. in2p3-00003400

HAL Id: in2p3-00003400

<https://hal.in2p3.fr/in2p3-00003400>

Submitted on 4 Nov 1998

HAL is a multi-disciplinary open access archive for the deposit and dissemination of scientific research documents, whether they are published or not. The documents may come from teaching and research institutions in France or abroad, or from public or private research centers.

L'archive ouverte pluridisciplinaire **HAL**, est destinée au dépôt et à la diffusion de documents scientifiques de niveau recherche, publiés ou non, émanant des établissements d'enseignement et de recherche français ou étrangers, des laboratoires publics ou privés.

A study of the hadronic resonance structure in the decay $\tau \rightarrow 3\pi\nu_\tau$

DELPHI Collaboration

Abstract

The hadronic structure of the decay of the τ lepton to three charged particles, $\tau \rightarrow 3\pi\nu_\tau$, is studied using data collected by the DELPHI detector at LEP between 1992 and 1995. The invariant mass of the 3π system, $m_{3\pi}$, is fitted using the models of Kühn and Santamaria, Isgur Morningstar and Reader, and Feindt. The 3π mass spectrum and the Dalitz projections are compared with each model. Below $m_{3\pi}^2 = 2.3 \text{ GeV}^2$, all are in good qualitative agreement. Above $m_{3\pi}^2 = 2.3 \text{ GeV}^2$, anomalous behaviour is observed, consistent with the existence of a hitherto unseen decay mode of the τ through a radial excitation of the a_1 meson.

(Submitted to Physics Letters B)

P.Abreu²¹, W.Adam⁴⁹, T.Adye³⁶, P.Adzic¹¹, G.D.Alekseev¹⁶, R.Aleman⁴⁸, P.P.Allport²², S.Almehed²⁴, U.Amaldi⁹, S.Amato⁴⁶, P.Andersson⁴³, A.Andreazza⁹, P.Antilogus²⁵, W-D.Apel¹⁷, Y.Arnoud¹⁴, B.Åsman⁴³, J-E.Augustin²⁵, A.Augustinus⁹, P.Baillon⁹, P.Bambade¹⁹, F.Barao²¹, G.Barbiellini⁴⁵, R.Barbier²⁵, D.Y.Bardin¹⁶, G.Barker⁹, A.Baroncelli³⁹, O.Barring²⁴, M.J.Bates³⁶, M.Battaglia¹⁵, M.Baubillier²³, K-H.Becks⁵¹, M.Begalli⁶, P.Beilliere⁸, Yu.Belokopytov^{9,52}, K.Belous⁴¹, A.C.Benvenuti⁵, C.Berat¹⁴, M.Berggren²⁵, D.Bertini²⁵, D.Bertrand², M.Besancon³⁸, F.Bianchi⁴⁴, M.Bigi⁴⁴, M.S.Bilenky¹⁶, M-A.Bizouard¹⁹, D.Bloch¹⁰, M.Bonesini²⁷, W.Bonivento²⁷, M.Boonekamp³⁸, P.S.L.Booth²², A.W.Borgland⁴, G.Borisov³⁸, C.Bosio³⁹, O.Botner⁴⁷, E.Boudinov³⁰, B.Bouquet¹⁹, C.Bourdarios¹⁹, T.J.V.Bowcock²², I.Boyko¹⁶, I.Bozovic¹¹, M.Bozzo¹³, P.Branchini³⁹, K.D.Brand³⁵, T.Brenke⁵¹, R.A.Brenner⁴⁷, R.Brown⁹, P.Bruckman³⁵, J-M.Brunet⁸, L.Bugge³², T.Buran³², T.Burgsmueller⁵¹, P.Buschmann⁵¹, S.Cabrera⁴⁸, M.Caccia²⁷, M.Calvi²⁷, A.J.Camacho Rozas⁴⁰, T.Camporesi⁹, V.Canale³⁷, M.Canepa¹³, F.Carena⁹, L.Carroll²², C.Caso¹³, M.V.Castillo Gimenez⁴⁸, A.Cattai⁹, F.R.Cavallo⁵, Ch.Cerruti¹⁰, V.Chabaud⁹, M.Chapkin⁴¹, Ph.Charpentier⁹, L.Chaussard²⁵, P.Checchia³⁵, G.A.Chelkov¹⁶, M.Chen², R.Chierici⁴⁴, P.Chliapnikov⁴¹, P.Chochula⁷, V.Chorowicz²⁵, J.Chudoba²⁹, K.Cieslik¹⁸, P.Collins⁹, M.Colomer⁴⁸, R.Contri¹³, E.Cortina⁴⁸, G.Cosme¹⁹, F.Cossutti⁹, J-H.Cowell²², H.B.Crawley¹, D.Crennell³⁶, G.Crosetti¹³, J.Cuevas Maestro³³, S.Czellar¹⁵, B.Dalmagne¹⁹, G.Damgaard²⁸, P.D.Dauncey³⁶, M.Davenport⁹, W.Da Silva²³, A.Deghorain², G.Della Ricca⁴⁵, P.Delpierre²⁶, N.Demaria⁹, A.De Angelis⁹, W.De Boer¹⁷, S.De Brabandere², C.De Clercq², B.De Lotto⁴⁵, A.De Min³⁵, L.De Paula⁴⁶, H.Dijkstra⁹, L.Di Ciaccio³⁷, A.Di Diodato³⁷, A.Djannati⁸, J.Dolbeau⁸, K.Doroba⁵⁰, M.Dracos¹⁰, J.Drees⁵¹, K.-A.Drees⁵¹, M.Dris³¹, A.Duperrin²⁵, J-D.Durand^{25,9}, D.Edsall¹, R.Ehret¹⁷, G.Eigen⁴, T.Ekelof⁴⁷, G.Ekspong⁴³, M.Ellert⁴⁷, M.Elsing⁹, J-P.Engel¹⁰, B.Erzen⁴², E.Falk²⁴, G.Fanourakis¹¹, D.Fassouliotis¹¹, J.Fayot²³, M.Feindt¹⁷, P.Ferrari²⁷, A.Ferrer⁴⁸, S.Fichet²³, A.Firestone¹, P.-A.Fischer⁹, U.Flagmeyer⁵¹, H.Foeth⁹, E.Fokitis³¹, F.Fontanelli¹³, B.Franek³⁶, A.G.Frodesen⁴, R.Fruhworth⁴⁹, F.Fulda-Quenzer¹⁹, J.Fuster⁴⁸, A.Galloni²², D.Gamba⁴⁴, M.Gandelman⁴⁶, C.Garcia⁴⁸, J.Garcia⁴⁰, C.Gaspar⁹, M.Gaspar⁴⁶, U.Gasparini³⁵, Ph.Gavillet⁹, E.N.Gazis³¹, D.Gele¹⁰, J-P.Gerber¹⁰, L.Gerdyukov⁴¹, N.Ghodbane²⁵, F.Gleze⁵¹, R.Gokiel⁵⁰, B.Golob⁴², P.Goncalves²¹, I.Gonzalez Caballero⁴⁰, G.Gopal³⁶, L.Gorn^{1,53}, M.Gorski⁵⁰, V.Gracco¹³, J.Grahl¹, E.Graziani³⁹, C.Green²², A.Grefrath⁵¹, P.Gris³⁸, G.Grosdidier¹⁹, K.Grzelak⁵⁰, M.Gunther⁴⁷, J.Guy³⁶, F.Hahn⁹, S.Hahn⁵¹, S.Haider⁹, A.Hallgren⁴⁷, K.Hamacher⁵¹, F.J.Harris³⁴, V.Hedberg²⁴, S.Heising¹⁷, R.Henriques²¹, J.J.Hernandez⁴⁸, P.Herquet², H.Herr⁹, T.L.Hessing³⁴, J.-M.Heuser⁵¹, E.Higon⁴⁸, S-O.Holmgren⁴³, P.J.Holt³⁴, D.Holthuizen³⁰, S.Hoorelbeke², M.Houlden²², J.Hrubic⁴⁹, K.Huet², K.Hultqvist⁴³, J.N.Jackson²², R.Jacobsson⁴³, P.Jalocha⁹, R.Janik⁷, Ch.Jarlskog²⁴, G.Jarlskog²⁴, P.Jarry³⁸, B.Jean-Marie¹⁹, E.K.Johansson⁴³, L.Jonsson²⁴, P.Jonsson²⁴, C.Joram⁹, P.Juillot¹⁰, F.Kapusta²³, K.Karafasoulis¹¹, S.Katsanevas²⁵, E.C.Katsoufis³¹, R.Keranen⁴, Yu.Khokhlov⁴¹, B.A.Khomenko¹⁶, N.N.Khovanski¹⁶, B.King²², N.J.Kjaer³⁰, O.Klapp⁵¹, H.Klein⁹, P.Kluit³⁰, D.Knoblach¹⁷, P.Kokkinias¹¹, M.Koratzinos⁹, V.Kostioukhine⁴¹, C.Kourkoumelis³, O.Kouznetsov¹⁶, M.Krammer⁴⁹, C.Kreuter⁹, I.Kronkvist²⁴, Z.Krumstein¹⁶, P.Kubinec⁷, W.Kucewicz¹⁸, K.Kurvinen¹⁵, C.Lacasta⁹, J.W.Lamsa¹, L.Lanceri⁴⁵, D.W.Lane¹, P.Langefeld⁵¹, J-P.Laugier³⁸, R.Lauhakangas¹⁵, G.Leder⁴⁹, F.Ledroit¹⁴, V.Lefebure², C.K.Legan¹, A.Leisos¹¹, R.Leitner²⁹, J.Lemonne², G.Lenzer⁵¹, V.Lepeltier¹⁹, T.Lesiak¹⁸, M.Lethuillier³⁸, J.Libby³⁴, D.Liko⁹, A.Lipniacka⁴³, I.Lippi³⁵, B.Loerstad²⁴, J.G.Loken³⁴, J.H.Lopes⁴⁶, J.M.Lopez⁴⁰, D.Loukas¹¹, P.Lutz³⁸, L.Lyons³⁴, J.MacNaughton⁴⁹, G.Maehlum¹⁷, J.R.Mahon⁶, A.Maio²¹, A.Malek⁵¹, T.G.M.Malmgren⁴³, V.Malychev¹⁶, F.Mandl⁴⁹, J.Marco⁴⁰, R.Marco⁴⁰, B.Marechal⁴⁶, M.Margoni³⁵, J-C.Marin⁹, C.Mariotti⁹, A.Markou¹¹, C.Martinez-Rivero³³, F.Martinez-Vidal⁴⁸, S.Marti i Garcia²², J.Masik²⁹, F.Matorras⁴⁰, C.Matteuzzi²⁷, G.Matthiae³⁷, F.Mazzucato³⁵, M.Mazzucato³⁵, M.Mc Cubbin²², R.Mc Kay¹, R.Mc Nulty⁹, G.Mc Pherson²², J.Medbo⁴⁷, C.Meroni²⁷, W.T.Meyer¹, A.Miagkov⁴¹, M.Michelotto³⁵, E.Migliore⁴⁴, L.Mirabito²⁵, W.A.Mitaroff⁴⁹, U.Mjoernmark²⁴, T.Moa⁴³, R.Moeller²⁸, K.Moenig⁹, M.R.Monge¹³, X.Moreau²³, P.Morettini¹³, H.Mueller¹⁷, K.Muenich⁵¹, M.Mulders³⁰, L.M.Mundim⁶, W.J.Murray³⁶, B.Muryn^{14,18}, G.Myatt³⁴, T.Myklebust¹², F.Naraghi¹⁴, F.L.Navarria⁵, S.Navas⁴⁸, K.Nawrocki⁵⁰, P.Negri²⁷, S.Nemecek¹², N.Neufeld⁹, W.Neumann⁵¹, N.Neumeister⁴⁹, R.Nicolaidou¹⁴, B.S.Nielsen²⁸, M.Nieuwenhuizen³⁰, V.Nikolaenko¹⁰, M.Nikolenko^{10,16}, P.Niss⁴³, A.Nomerotski³⁵, A.Normand²², A.Nygren²⁴, W.Oberschulte-Beckmann¹⁷, V.Obraztsov⁴¹, A.G.Olshevski¹⁶, A.Onofre²¹, R.Orava¹⁵, G.Orazi¹⁰, K.Osterberg¹⁵, A.Ouraou³⁸, P.Paganini¹⁹, M.Paganoni²⁷, S.Paiano⁵, R.Pain²³, R.Paiva²¹, H.Palka¹⁸, Th.D.Papadopoulou³¹, K.Papageorgiou¹¹, L.Pape⁹, C.Parkes³⁴, F.Parodi¹³, U.Parzefall²², A.Passeri³⁹, M.Pegoraro³⁵, L.Peralta²¹, H.Pernegger⁴⁹, M.Pernicka⁴⁹, A.Perrotta⁵, C.Petridou⁴⁵, A.Petrolini¹³, H.T.Phillips³⁶, G.Piana¹³, F.Pierre³⁸, M.Pimenta²¹, E.Piotto³⁵, T.Podobnik³⁴, O.Podobrin⁹, M.E.Pol⁶, G.Polok¹⁸, P.Poropat⁴⁵, V.Pozdniakov¹⁶, P.Privitera³⁷, N.Pukhaeva¹⁶, A.Pullia²⁷, D.Radojicic³⁴, S.Ragazzi²⁷, H.Rahmani³¹, D.Rakoczy⁴⁹, P.N.Ratoff²⁰, A.L.Read³², P.Rebecchi⁹, N.G.Redaeli²⁷, M.Regler⁴⁹, D.Reid⁹, R.Reinhardt⁵¹, P.B.Renton³⁴, L.K.Resvanis³, F.Richard¹⁹, J.Ridky¹², G.Rinaudo⁴⁴, O.Rohne³², A.Romero⁴⁴, P.Ronchese³⁵, E.I.Rosenberg¹, P.Rosinsky⁷, P.Roudeau¹⁹, T.Rovelli⁵, V.Ruhlmann-Kleider³⁸, A.Ruiz⁴⁰, H.Saarikko¹⁵, Y.Sacquin³⁸, A.Sadovsky¹⁶, G.Sajot¹⁴, J.Salt⁴⁸, D.Sampsonidis¹¹, M.Sannino¹³, H.Schneider¹⁷, Ph.Schwemling²³, U.Schwickerath¹⁷, M.A.E.Schyns⁵¹, F.Scuri⁴⁵, P.Seager²⁰, Y.Sedykh¹⁶, A.M.Segar³⁴, R.Sekulin³⁶, R.C.Shellard⁶, A.Sheridan²², R.Silvestre³⁸, F.Simonetto³⁵, A.N.Sisakian¹⁶, T.B.Skaali³², G.Smadja²⁵, N.Smirnov⁴¹, O.Smirnova²⁴, G.R.Smith³⁶, A.Sokolov⁴¹, O.Solovianov⁴¹, A.Sopczak¹⁷, R.Sosnowski⁵⁰, D.Souza-Santos⁶, T.Spaso²¹, E.Spiriti³⁹, P.Sponholz⁵¹, S.Squarcia¹³, D.Stampfer⁴⁹, C.Stanescu³⁹, S.Stanic⁴², S.Stapnes³², I.Stavitski³⁵, K.Stevenson³⁴, A.Stocchi¹⁹, J.Strauss⁴⁹, R.Strub¹⁰, B.Stugu⁴, M.Szczekowski⁵⁰, M.Szeptycka⁵⁰, T.Tabarelli²⁷, F.Tegenfeldt⁴⁷, F.Terranova²⁷

J.Thomas³⁴, A.Tilquin²⁶, J.Timmermans³⁰, L.G.Tkatchev¹⁶, T.Todorov¹⁰, S.Todorova¹⁰, D.Z.Toet³⁰, A.Tomaradze², B.Tome²¹, A.Tonazzo²⁷, L.Tortora³⁹, G.Transtrome²⁴, D.Treille⁹, G.Tristram⁸, A.Trombini¹⁹, C.Troncon²⁷, A.Tsirou⁹, M-L.Turluer³⁸, I.A.Tyapkin¹⁶, M.Tyndel³⁶, S.Tzamarias¹¹, B.Ueberschaer⁵¹, O.Ullaland⁹, V.Uvarov⁴¹, G.Valenti⁵, E.Vallazza⁴⁵, G.W.Van Apeldoorn³⁰, P.Van Dam³⁰, W.K.Van Doninck², J.Van Eldik³⁰, A.Van Lysebetten², I.Van Vulpen³⁰, N.Vassilopoulos³⁴, G.Vegni²⁷, L.Ventura³⁵, W.Venus³⁶, F.Verbeure², M.Verlato³⁵, L.S.Vertogradov¹⁶, V.Verzi³⁷, D.Vilanova³⁸, L.Vitale⁴⁵, E.Vlasov⁴¹, A.S.Vodopyanov¹⁶, V.Vrba¹², H.Wahlen⁵¹, C.Walck⁴³, C.Weiser¹⁷, A.M.Wetherell⁹, D.Wicke⁵¹, J.H.Wickens², M.Wielers¹⁷, G.R.Wilkinson⁹, W.S.C.Williams³⁴, M.Winter¹⁰, M.Witek¹⁸, T.Wlodek¹⁹, G.Wolf⁹, J.Yi¹, O.Yushchenko⁴¹, A.Zaitsev⁴¹, A.Zalewska¹⁸, P.Zalewski⁵⁰, D.Zavrtanik⁴², E.Zevgolatakos¹¹, N.I.Zimin¹⁶, G.C.Zucchelli⁴³, G.Zumerle³⁵

¹Department of Physics and Astronomy, Iowa State University, Ames IA 50011-3160, USA

²Physics Department, Univ. Instelling Antwerpen, Universiteitsplein 1, BE-2610 Wilrijk, Belgium and IIHE, ULB-VUB, Pleinlaan 2, BE-1050 Brussels, Belgium

and Faculté des Sciences, Univ. de l'Etat Mons, Av. Maistriau 19, BE-7000 Mons, Belgium

³Physics Laboratory, University of Athens, Solonos Str. 104, GR-10680 Athens, Greece

⁴Department of Physics, University of Bergen, Allégaten 55, NO-5007 Bergen, Norway

⁵Dipartimento di Fisica, Università di Bologna and INFN, Via Irnerio 46, IT-40126 Bologna, Italy

⁶Centro Brasileiro de Pesquisas Físicas, rua Xavier Sigaud 150, BR-22290 Rio de Janeiro, Brazil

and Depto. de Física, Pont. Univ. Católica, C.P. 38071 BR-22453 Rio de Janeiro, Brazil

and Inst. de Física, Univ. Estadual do Rio de Janeiro, rua São Francisco Xavier 524, Rio de Janeiro, Brazil

⁷Comenius University, Faculty of Mathematics and Physics, Mlynska Dolina, SK-84215 Bratislava, Slovakia

⁸Collège de France, Lab. de Physique Corpusculaire, IN2P3-CNRS, FR-75231 Paris Cedex 05, France

⁹CERN, CH-1211 Geneva 23, Switzerland

¹⁰Institut de Recherches Subatomiques, IN2P3 - CNRS/ULP - BP20, FR-67037 Strasbourg Cedex, France

¹¹Institute of Nuclear Physics, N.C.S.R. Demokritos, P.O. Box 60228, GR-15310 Athens, Greece

¹²FZU, Inst. of Phys. of the C.A.S. High Energy Physics Division, Na Slovance 2, CZ-180 40, Praha 8, Czech Republic

¹³Dipartimento di Fisica, Università di Genova and INFN, Via Dodecaneso 33, IT-16146 Genova, Italy

¹⁴Institut des Sciences Nucléaires, IN2P3-CNRS, Université de Grenoble 1, FR-38026 Grenoble Cedex, France

¹⁵Helsinki Institute of Physics, HIP, P.O. Box 9, FI-00014 Helsinki, Finland

¹⁶Joint Institute for Nuclear Research, Dubna, Head Post Office, P.O. Box 79, RU-101 000 Moscow, Russian Federation

¹⁷Institut für Experimentelle Kernphysik, Universität Karlsruhe, Postfach 6980, DE-76128 Karlsruhe, Germany

¹⁸Institute of Nuclear Physics and University of Mining and Metallurgy, Ul. Kawory 26a, PL-30055 Krakow, Poland

¹⁹Université de Paris-Sud, Lab. de l'Accélérateur Linéaire, IN2P3-CNRS, Bât. 200, FR-91405 Orsay Cedex, France

²⁰School of Physics and Chemistry, University of Lancaster, Lancaster LA1 4YB, UK

²¹LIP, IST, FCUL - Av. Elias Garcia, 14-1^o, PT-1000 Lisboa Codex, Portugal

²²Department of Physics, University of Liverpool, P.O. Box 147, Liverpool L69 3BX, UK

²³LPNHE, IN2P3-CNRS, Univ. Paris VI et VII, Tour 33 (RdC), 4 place Jussieu, FR-75252 Paris Cedex 05, France

²⁴Department of Physics, University of Lund, Sölvegatan 14, SE-223 63 Lund, Sweden

²⁵Université Claude Bernard de Lyon, IPNL, IN2P3-CNRS, FR-69622 Villeurbanne Cedex, France

²⁶Univ. d'Aix - Marseille II - CPP, IN2P3-CNRS, FR-13288 Marseille Cedex 09, France

²⁷Dipartimento di Fisica, Università di Milano and INFN, Via Celoria 16, IT-20133 Milan, Italy

²⁸Niels Bohr Institute, Blegdamsvej 17, DK-2100 Copenhagen Ø, Denmark

²⁹NC, Nuclear Centre of MFF, Charles University, Areal MFF, V Holesovickach 2, CZ-180 00, Praha 8, Czech Republic

³⁰NIKHEF, Postbus 41882, NL-1009 DB Amsterdam, The Netherlands

³¹National Technical University, Physics Department, Zografou Campus, GR-15773 Athens, Greece

³²Physics Department, University of Oslo, Blindern, NO-1000 Oslo 3, Norway

³³Dpto. Física, Univ. Oviedo, Avda. Calvo Sotelo s/n, ES-33007 Oviedo, Spain, (CICYT-AEN96-1681)

³⁴Department of Physics, University of Oxford, Keble Road, Oxford OX1 3RH, UK

³⁵Dipartimento di Fisica, Università di Padova and INFN, Via Marzolo 8, IT-35131 Padua, Italy

³⁶Rutherford Appleton Laboratory, Chilton, Didcot OX11 0QX, UK

³⁷Dipartimento di Fisica, Università di Roma II and INFN, Tor Vergata, IT-00173 Rome, Italy

³⁸DAPNIA/Service de Physique des Particules, CEA-Saclay, FR-91191 Gif-sur-Yvette Cedex, France

³⁹Istituto Superiore di Sanità, Ist. Naz. di Fisica Nucl. (INFN), Viale Regina Elena 299, IT-00161 Rome, Italy

⁴⁰Instituto de Física de Cantabria (CSIC-UC), Avda. los Castros s/n, ES-39006 Santander, Spain, (CICYT-AEN96-1681)

⁴¹Inst. for High Energy Physics, Serpukov P.O. Box 35, Protvino, (Moscow Region), Russian Federation

⁴²J. Stefan Institute, Jamova 39, SI-1000 Ljubljana, Slovenia and Department of Astroparticle Physics, School of Environmental Sciences, Kostanjevska 16a, Nova Gorica, SI-5000 Slovenia,

and Department of Physics, University of Ljubljana, SI-1000 Ljubljana, Slovenia

⁴³Fysikum, Stockholm University, Box 6730, SE-113 85 Stockholm, Sweden

⁴⁴Dipartimento di Fisica Sperimentale, Università di Torino and INFN, Via P. Giuria 1, IT-10125 Turin, Italy

⁴⁵Dipartimento di Fisica, Università di Trieste and INFN, Via A. Valerio 2, IT-34127 Trieste, Italy

and Istituto di Fisica, Università di Udine, IT-33100 Udine, Italy

⁴⁶Univ. Federal do Rio de Janeiro, C.P. 68528 Cidade Univ., Ilha do Fundão BR-21945-970 Rio de Janeiro, Brazil

⁴⁷Department of Radiation Sciences, University of Uppsala, P.O. Box 535, SE-751 21 Uppsala, Sweden

⁴⁸IFIC, Valencia-CSIC, and D.F.A.M.N., U. de Valencia, Avda. Dr. Moliner 50, ES-46100 Burjassot (Valencia), Spain

⁴⁹Institut für Hochenergiephysik, Österr. Akad. d. Wissensch., Nikolsdorfergasse 18, AT-1050 Vienna, Austria

⁵⁰Inst. Nuclear Studies and University of Warsaw, Ul. Hoza 69, PL-00681 Warsaw, Poland

⁵¹Fachbereich Physik, University of Wuppertal, Postfach 100 127, DE-42097 Wuppertal, Germany

⁵²On leave of absence from IHEP Serpukhov

⁵³Now at University of Florida

1 Introduction

The structure of the decay of the τ to three charged pions, $\tau \rightarrow 3\pi\nu_\tau$, has been the subject of much theoretical and experimental effort. It allows the weak hadronic current to be investigated and the parity violating asymmetry parameter to be determined. In addition, light-meson spectroscopy can be studied. An understanding of the mass spectrum is also important if this channel is to be used to measure the τ neutrino mass.

In the decay $\tau \rightarrow 3\pi\nu_\tau$, the 3π system is expected to have the quantum numbers $J^{PC} = 1^{++}$, with some small contribution of 0^{-+} , and to be produced predominantly via the a_1 resonance. However, many problems still exist, both in the determination of the mass and width of the a_1 meson, and in the mechanism by which the τ decays to three pions. Experiments measuring the a_1 meson parameters from direct production in hadronic interactions obtain lower values for the mass and width than those which measure them in τ decays². Values obtained from τ data alone also vary, being dependent on the model and decay mechanism which are assumed. Section 2 briefly discusses three models which this paper considers.

LEP provides an ideal environment for the study of τ pairs, which can be detected with high efficiency and low background. The various channels into which the τ decays can be distinguished with good purity and efficiency using the DELPHI detector, which is described in section 3. Section 4 describes how a sample of precisely reconstructed events from the decay $\tau \rightarrow 3\pi\nu_\tau$ can be separated from other τ decays. Due to the excellent tracking detectors and in particular the presence of silicon microvertex detectors, the invariant mass of the three pion system can be measured with a typical precision of 20 MeV. The high purity and precise mass measurement allow various models to be compared. Section 5 describes the fits to the models while results and discussions are presented in section 6 and conclusions in section 7.

2 Theoretical Models

The models of Kühn and Santamaria [2] (KS), Isgur Morningstar and Reader [3] (IMR), and Feindt [4] have been reasonably successful in describing the decay $\tau \rightarrow 3\pi\nu_\tau$. All assume that the decay proceeds predominantly through the a_1 resonance.

The KS model allows the τ to decay to a_1 which then decays simply to a mixture of $\rho\pi$ and $\rho(1450)\pi$ which exist in the lowest dimensional Born state (approximately the S-wave state). The resonances are parameterised as Breit-Wigner functions with energy dependent widths. Constant form-factors are employed in describing the $a_1 \rightarrow \rho\pi$ and $\rho \rightarrow \pi\pi$ vertices.

The IMR model allows the τ to decay to the axial-vector a_1 and the pseudo-scalar $\pi(1300)$. The a_1 decays through both D-wave and S-wave $\rho\pi$ states, as well as through the K^*K channel. The $\pi(1300)$ decays to $\rho\pi$ and through a broad $\pi\pi$ S-wave state. In addition, the model makes use of a three parameter polynomial background term which was found necessary in order to “take into account many possible small effects ... e.g., the low-mass tails of radial excitations of the a_1 and ρ ” [3]. Another very significant difference from KS is the employment of strong, energy dependent form-factors. These affect the mass dependent width of the a_1 in different ways: in KS the width increases with s (Fig. 2 of [2]); in IMR it increases to a maximum at $s \approx 1.4$ after which it decreases (Fig. 8 of [3]). It is principally this effect which causes the large differences in the masses and widths of the a_1 [5] measured in τ decays.

²See the review of $a_1(1260)$ on page 345 of PDG 1996 and references therein [1].

The Feindt model is similar to the KS and IMR models but has a more general form, allowing any combination of intermediate resonances and spin states. By appropriate selection of decay channels and form-factors, it can be made to resemble either KS or IMR. This versatility is particularly useful in evaluating the effects of different combinations of decay channels.

3 The DELPHI detector

DELPHI is well suited to this analysis, having excellent tracking components and good photon identification. The detector is described in detail elsewhere [6,7]. This section briefly describes the sub-detectors used in this analysis.

Charged particles are measured in the tracking detectors which are situated inside a 1.2 T super-conducting solenoid. The main tracking chamber is a time projection chamber (TPC) situated between radii of 35 cm and 120 cm. It reconstructs tracks with a typical precision in the $R\phi$ plane³ of 300 μm , and in the Rz plane of 1 mm. Inside the TPC, between radii of 12 cm and 35 cm, is the Inner Detector (ID), a jet chamber with a typical $R\phi$ precision of 60 μm . Outside the TPC, between radii of 200 cm and 210 cm, is the Outer Detector (OD) which has an effective $R\phi$ precision of 300 μm . Close to the interaction region, lies the microvertex detector (μVD) which consists of three planes of silicon strip detectors at radii of 6.3, 9.0 and 11.0 cm. They have an $R\phi$ precision of 7 μm and a two track resolution of 100 μm .

Tracks reconstructed with all four detector elements have a momentum precision of $\delta(1/p_t) = 8 \times 10^{-4} (\text{GeV})^{-1}$ and a track extrapolation precision close to the interaction region of $23 \oplus 55p^{-1}(\sin\theta)^{-1.5} \mu\text{m}$, where p and p_t are the momentum and transverse momentum in GeV and θ is the polar angle.

Outside the tracking chambers are the electro-magnetic and hadronic calorimeters. The electro-magnetic calorimeter (HPC), situated between radii of 210 cm and 240 cm, provides measurements of both the energy and position of a shower. The energy resolution is measured to be $\delta E/E = 0.31 \times (E/\text{GeV})^{-0.44} \oplus 0.027$ while the spatial precision is 1 mrad in polar angle and 2 mrad in azimuthal angle.

The hadron calorimeter is situated outside the solenoid coil and presents nine interaction lengths of iron. Outside this lie the muon chambers wherein a hit usually signifies the presence of a muon.

4 Selection of the Decay $\tau \rightarrow 3\pi\nu_\tau$

This analysis uses data taken between 1992 and 1995, corresponding to about 3.5 million hadronic Z decays, or about 170,000 τ pairs. The selection of $\tau \rightarrow 3\pi\nu_\tau$ candidates starts by identifying decays of the Z to two τ leptons produced back to back, one of which decays to three charged particles, while the other decays to one or three charged particles.

Two hemispheres are defined relative to the thrust axis, and at least one hemisphere is required to contain three tracks which are each isolated by at least 160° from all tracks in the other hemisphere. The following conditions are then placed on the three tracks in order to reduce backgrounds. The vector sum of their momenta must exceed 10 GeV. The total electro-magnetic energy in a cone of 15° about the vector sum of their momenta must be less than half their summed momenta. The typical signature of a π^0 in DELPHI is

³ R, ϕ and z define a polar co-ordinate system with the origin at the interaction point and the z axis along the electron direction.

either two neutral electro-magnetic clusters, or one high energy neutral deposit [7]. Thus to reject $\tau \rightarrow \pi\pi\pi(n\pi^0)\nu_\tau$ decays, events having two or more neutral energy deposits greater than 500 MeV or events with a single deposit greater than 2 GeV are rejected. The event is also removed if any of the three tracks points to hits in the muon chambers and has deposits in the hadron calorimeter consistent with a minimum ionising particle. Such events may originate from four-fermion processes.

The track reconstruction algorithm closely follows that used in the DELPHI determination of the τ lifetime [8], with tight requirements on both track and vertex reconstruction quality. Starting from the TPC track elements, extrapolations are made inwards to the μ VD, where all possible hit combinations are considered. ID and OD elements are added to the candidate tracks where possible. All three tracks are required to have at least two hits in the μ VD, which effectively confines this analysis to the barrel region of DELPHI. A vertex fit is performed in the transverse plane, for every combination of candidate tracks. It is required that only one combination of track elements has a track fit and vertex fit probability above 1%. This cut is chosen because the distributions are flat above this value, and rise sharply below it due to random combinations. The reconstructed vertex is required to lie within 3 cm of the beam-spot, in order to reject photon conversions in the beam-pipe.

The invariant mass squared s of the 3π system and its reconstruction error σ_s are calculated at the vertex assuming the pion mass for all the particles. The error on \sqrt{s} is typically between 10 and 35 MeV with an average of 22 MeV for a mass of 1.2 GeV, and between 15 and 55 MeV with an average of 36 MeV for a mass of 1.6 GeV. The invariant mass squared of pairs of oppositely charged particles is found assuming the pion mass. In total, 7180 events remain after all cuts.

The selection requirements for identifying the decay $\tau \rightarrow 3\pi\nu_\tau$ were chosen considering the various background processes, both from other τ decays involving kaons or unidentified π^0 s and from non- τ sources. These contributions were estimated using Monte Carlo simulations. The KORALZ generator [9] with the TAUOLA 2.5 decay package [10] was used to produce τ decays which were passed through a full detector simulation. The branching ratio of each channel was re-weighted to the world-average value [1], except for the kaon channels where recent DELPHI results were used [11]. The $3\pi\pi^0$ channel was modified by including the process $\tau \rightarrow \rho\pi\pi\nu_\tau$ where the pions have opposite charge. Contamination from non- τ sources comes from hadronic decays of the Z and from four-fermion events. Both were estimated from simulation. The hadronic Z decays were generated using the JETSET Parton Shower model [12], and the four-fermion events using the BDK generator [13]. The efficiency inside $|\cos\theta| < 0.73$ was found to be 36% with a background of 20%, whose composition is detailed in Table 1. Note, however, that the background is not flat in s ; at high values, the sample is essentially pure.

5 Comparisons with KS and IMR models

This section describes the fitting of the distribution of the invariant mass squared of the three pions to the models of KS and IMR and the extraction of the a_1 parameters. The Dalitz plots are compared with the predictions of both models. Anomalous behaviour in the high s region leads to some discussion of possible causes.

5.1 Fits to the invariant mass squared distribution

The distribution of the invariant mass squared s of the three pions is fitted to the models by maximising the likelihood function L :

$$L = \sum_{i=1}^{bins} n_i \log \mu_i - \mu_i \quad (1)$$

where the sum runs over all bins, with n_i being the number of observed events in mass bin i and μ_i the predicted number of events. The predicted shape is the sum of signal, $P_{sig}(s)$, and background, $P_{bkg}(s)$. The shape and proportion of the background are taken from simulation. $P_{sig}(s)$ is obtained from the theoretical model distribution $T(s)$ corrected for resolution and efficiency effects.

$$P_{sig}(s) = \epsilon(s) \int ds' T(s') \int d\sigma D(\sigma, s) R(s, s', \sigma) \quad (2)$$

where $\epsilon(s)$ is the efficiency taken from the simulation, $D(\sigma, s)$ is the distribution of σ at a given s , and $R(s, s_{true}, \sigma)$ is the resolution function obtained from the simulation. It was found by plotting $(s - s_{true})/\sigma$, which is well parameterised by three Gaussian functions of widths 1, 3, and 7 and weights 0.950, 0.045, and 0.005 respectively.

Results for the following models are presented:

- the KS model, with parameters and masses as given in the first row of Table 1 of [2]. The mass and width of the a_1 meson are left as free parameters.
- the IMR model, where the prescription for their ‘preferred’ fit is followed but the KK^* contributions are not included as they do not contain 3π in the final state⁴. The PDG values [1] are taken for all masses and widths. The strong decay on-shell form factors are taken from the model predictions detailed in Appendix B of [3]. The mass of the a_1 meson and the three terms characterising the polynomial background are left as free parameters. The a_1 width is calculated from the a_1 mass in accordance with the model.

The fits are shown in Fig. 1a) and b); the a_1 parameters are given in the columns labelled ‘KS’ and ‘IMR with polynomial’ of Table 2; a feeling for the goodness of fit is given in Table 3.

The data are in reasonably good agreement with the KS model. The χ^2 over the 27 bins from $s = 0.5 \text{ GeV}^2$ to $s = 3.2 \text{ GeV}^2$ is 32. Close to the endpoint, however, the data lie somewhat higher than the model predicts; the poorer χ^2 in the end-region reflects this. The mass and width of the a_1 are measured to be $1255 \pm 7 \text{ MeV}$ and $587 \pm 27 \text{ MeV}$ respectively, which agree with previous experimental determinations [14,15]. It is noteworthy, however, that these results predict [2] a branching ratio $BR(\tau \rightarrow 3\pi\nu_\tau) = 6.6 \pm 0.3\%$, in disagreement with the direct measurement of this quantity of $8.8 \pm 0.1\%$ ⁵.

The IMR model is also in reasonable agreement with the data. The χ^2 over the 27 bins from $s = 0.5 \text{ GeV}^2$ to $s = 3.2 \text{ GeV}^2$ is 36. The mass of the a_1 is measured to be $1207 \pm 5 \text{ MeV}$ and the width is calculated to be $478 \pm 3 \text{ MeV}$. This is in agreement with previous experimental determinations, noting that the small statistical error on the width is due to holding the form factors fixed at their theoretical values whereas other experiments have chosen to fit for them.

The polynomial term contributes 2% of the total 3π decay rate. However, it gives one third (half) of the contribution above $s = 2.5$ (2.7) GeV^2 . This could be taken as

⁴The effect of the KK^* channel, where the final state kaons are mis-identified as pions, is considered below when estimating the backgrounds.

⁵This has been calculated by subtracting the kaon channels [11] from the branching ratio for $\tau \rightarrow 3h\nu_\tau$ [1].

a qualitative indication of the existence of some higher mass resonance. Results for the fit without the polynomial background term are given in Tables 2 and 3 in the column labelled ‘IMR without polynomial’. The fitted mass rises to 1217 MeV but a poorer fit is obtained, especially in the end-point region where a χ^2 of 40 is found for the 12 bins between $s = 2.0 \text{ GeV}^2$ and 3.2 GeV^2 .

A number of systematic uncertainties which affect the determination of the a_1 parameters have been considered.

The modelling of the background from other τ decays was investigated. In the $3\pi\pi^0$ channel, the mass and width of the ρ' were varied from their default values of 1.45 GeV and 0.30 GeV respectively, to a mass of 1.70 GeV and a width of 0.26 GeV (parameters of the $\rho(1700)$ [1]), and also to the parameterisation as given in [16]. Furthermore, the channel $\tau \rightarrow \rho\pi\pi\nu_\tau$ which had been added to the TAUOLA defaults was removed. In addition the overall normalisation was changed by 9%, which was the largest deviation in efficiency between data and simulation observed in the selection procedure. The normalisation of the kaon channels was varied by 30%. Systematic errors from these sources of 5 and 8 MeV for the mass, and 18 and 3 MeV for the width, were found for the KS and IMR models respectively.

The detector resolution was checked by reconstructing the D^0 mass peak from a data sample of D^* mesons which decay via $D^* \rightarrow D^0\pi \rightarrow K\pi\pi$. The mass and momentum spectrum of the D^0 are similar to those of the τ . The mass peak was fitted using the nominal 3-Gaussian resolution function described above, together with a scale factor k_1 to multiply the calculated σ and a second factor k_2 to multiply the proportion of the second Gaussian. The values obtained are $k_1 = 1.04 \pm 0.04$, $k_2 = 1.7 \pm 0.5$. These values were used to calculate a systematic uncertainty. Errors from these sources of 3 and 2 MeV for the mass, and 11 and 1 MeV for the width were found for KS and IMR respectively. An additional systematic of 15 MeV is included on the a_1 width in the IMR model, due to the variations in the form factors (as given in [3]) which come from varying the string-breaking constant γ_0 from its nominal value of 0.39 [17] within its rounding error of 0.005.

5.2 The Dalitz plots and projections

Holding the parameters fixed at the values given by the relevant fits, the Dalitz plots in various s ranges are shown in the first three columns of Fig. 2 for data, KS, and the resonant part of IMR (since the shape the polynomial background would assume is unknown). The quantities s_1 and s_2 are the invariant mass squared values for the two unlike-sign two-particle combinations, with $s_1 > s_2$. The distributions for the models include resolution and efficiency effects, but not the effects of non- $\tau \rightarrow 3\pi$ backgrounds.

In the two lower s ranges displayed, the structures apparent in the data appear to be well reproduced by both models.

In the two higher s bins, however, the prominent ρ bands of the KS model, such that the Dalitz plot density reaches a maximum where they cross, are no longer well reproduced in the data. The double peaked structure of the IMR model appears to provide a much better agreement with the data, although the normalisation (which is not apparent in the Dalitz plots) is very different. This double peaked structure is due to the energy dependent form-factors which, for IMR, create the $\rho\pi$ predominantly in a D-wave state at high values of s , whereas KS assumes an approximate S-wave state at all energies

To judge the agreement between the data and the models better, the Dalitz plots are projected onto their axes ⁶ in Fig. 3. The normalisation is now clear, and the background contributions that the simulations predict have been included. To evaluate the goodness of fit, the χ^2 and number of bins are given for each s region in Table 3.

Below $s = 2.3 \text{ GeV}^2$, Fig. 3 confirms that both models give good qualitative agreement. They reproduce a ρ peak in about the correct position and show that the dominant decay mode proceeds via $\tau \rightarrow a_1\nu_\tau \rightarrow \rho\pi\nu_\tau \rightarrow \pi\pi\pi\nu_\tau$. As pointed out previously by OPAL [14] and ARGUS [15], the agreement is not perfect and there is some evidence of minor discrepancies. Relatively small modifications to the models may explain these discrepancies; for example, IMR describe possible mass shift functions and KS enter into some discussion on the parameterisation of the Breit-Wigner functions. Some of the large χ^2 values in Table 3 could be reconciled by a simple shift of the ρ peak. There is also some indication of an ω peak (in Figs. 3 and 4, sub-plots ‘d’ and ‘e’ for $\sqrt{s_1}$ and sub-plot ‘c’ for $\sqrt{s_2}$), whose effect is not included in the models or in the simulation.

Above $s = 2.3 \text{ GeV}^2$, where an excess of events is observed in the s distribution, the first Dalitz projection in Fig. 3 shows an excess of events at $\sqrt{s_1}$ of about 1.25 GeV, in disagreement with the models.

5.3 Discussion

Taking into account phase space effects, the enhancement observed at $\sqrt{s_1}$ of about 1.25 GeV for s above 2.3 GeV^2 could be explained by a decay channel of the τ to a resonance of mass similar to or greater than the τ mass which then decays to 3π through the intermediate state of a pion plus a particle of mass 1.25 GeV or greater.

An excellent candidate for this resonance is the a'_1 , which is a radial excitation of the a_1 meson. It is predicted in the flux-tube breaking model of Isgur and Kokoski [17] to have a mass of 1820 MeV and to decay to the $\rho(770)\pi$ D-wave state in preference to the S-wave state. Such a resonance has probably already been seen by the VES collaboration [18], which reported a clear signal in the D-wave state (and an enhancement of equal size in the S-wave), for a $J^{PC} = 1^{++}$ particle with a mass of about 1700 MeV and a width of about 300 MeV. If this exists, then there is every reason to expect it to be present in τ decays, and in fact Iizuka et al. [19] have already postulated such a particle as a means of reconciling the discrepancy in the a_1 parameters measured in hadronic experiments and in τ decays. Furthermore, Shuryak and Kapusta [20] use Weinberg sum rules to relate the vector and axial-vector τ decay modes and conclude that there is a missing contribution in the axial-vector mode which could be explained by an a'_1 .

A similar signal was also reported by the VES collaboration in the 1^{++} wave in the $f_1\pi$ channel [21]. If this is due to the decay of the same resonance, one might expect an enhanced production of $f_1\pi$ in τ decays. This is exactly what CLEO reported recently [22], with the first observation of the decay $\tau \rightarrow f_1\pi\nu_\tau$, at a level in excess of theoretical prediction. If it is assumed that the same resonance is responsible for the VES, CLEO and DELPHI signals, then a branching ratio for $\tau \rightarrow a'_1\nu_\tau \rightarrow 3\pi\nu_\tau$ of order 10^{-3} can be predicted from CLEO’s reported branching ratio and the relative probabilities which VES observe for the decays of this resonance to $f_1\pi$, $(3\pi)_S$ and $(3\pi)_D$.

⁶Projection onto the $s_1 + s_2$ axis would show the discrepancy more clearly, but at some cost in transparency.

6 Studies with the Feindt model

Following on from the discussions above, the extra versatility of the Feindt model is now used to introduce an a'_1 resonance. First though, in order to make contact with the models already discussed, an attempt is made to make the Feindt model look like the previous two models. The results are given in Table 2 and the goodness of fit in Table 3.

In the first fit (MF-KS₀), the a_1 is assumed to decay, as in the KS prescription, to $\rho\pi$ and $\rho'\pi$ states using constant form-factors and a monotonically increasing energy dependent width. A fit is made for both the mass and width of the a_1 , giving values of 1265 MeV and 607 MeV respectively, close to but not identical to the results of KS.

In the second fit (MF-IMR₀), the a_1 is assumed to decay, as in the IMR prescription, to S- and D-wave $\rho\pi$ states using the strong form-factors and the energy dependent width predicted by this model. The polynomial background term is not used. The mass and width are fitted; this is different from IMR, where the width was derived as a function of the mass. The mass and width are measured to be 1213 MeV and 476 MeV respectively, consistent with the results for IMR without the polynomial term.

The Feindt model is then modified so that, in addition to the decays through the a_1 , the τ is allowed to decay through an a'_1 . The complex Breit-Wigner function (BW) which described the amplitude of the a_1 resonance, is modified by an admixture of a'_1 :

$$BW_a \rightarrow BW_a + \kappa e^{i\phi} BW_{a'_1}. \quad (3)$$

The a'_1 is described by a BW with a mass of 1700 MeV and a width of 300 MeV, and is allowed to decay with equal probability into the S-wave $\rho(1450)\pi$ state and the D-wave $\rho(770)\pi$ state, as suggested by the predictions of Isgur and Kokoski and the experimental VES results.

Two further fits are then made: in the first (MF-KS₁) the underlying KS description (MF-KS₀) is modified by the addition of an a'_1 ; in the second (MF-IMR₁), it is the IMR description (MF-IMR₀) which is changed. These further fits are made to both the s distribution and the two Dalitz projections for the regions $2.0 \text{ GeV}^2 < s < 2.3 \text{ GeV}^2$ and $2.3 \text{ GeV}^2 < s < 3.2 \text{ GeV}^2$. The mass and width of the a_1 are left as free parameters as well as the admixture κ and phase ϕ of the a'_1 contribution.

The results of the fits are given in Table 2. Note that the fitted widths of the a_1 are both lower than those obtained before adding an a'_1 , while the fitted mass of the a_1 is lower for MF-IMR₁ than for MF-IMR₀. Since the only difference between MF-KS₀ and MF-KS₁, or between MF-IMR₀ and MF-IMR₁, is the addition of a small amount of a'_1 , it is observed that the a_1 mass and width are sensitive to the addition of higher mass resonances in the 3π spectrum. This might help explain the discrepancy between the parameters of the a_1 measured in τ decay and in hadronic production.

The fits to the s distribution are shown in Figs. 1c) and d). As shown in Table 3, the χ^2 values over the 27 bins from $s = 0.5 \text{ GeV}^2$ to $s = 3.2 \text{ GeV}^2$ are 28 for MF-KS₁ and 25 for MF-IMR₁, which are better than those for previous fits. In the high s region, the χ^2 values for the 12 bins between $s = 2.0 \text{ GeV}^2$ and $s = 3.2 \text{ GeV}^2$ improve to 13 for MF-KS₁ and 11 for MF-IMR₁.

The Dalitz plots are shown in the last two columns of Fig. 2. MF-IMR₁ shows the same characteristics in the high s plots as the data. The agreement of MF-KS₁ is less striking, but better than KS. The projections are shown in Fig. 4, while the goodness of fit in each of the histograms is given in Table 3. The improvements in the high s bins are marked. In the lower s bins, the goodness of fit is roughly similar to that of the original fits for MF-IMR, but is worse for MF-KS due to an induced shift in the ρ peak.

In the absence of interference effects, the percentage of decays, P , which proceed via the a'_1 and a_1 can be calculated by the following integral over phase-space:

$$P(A) = \frac{\kappa_A^2 \int dLIPS BW_A(s) BW_A(s)^*}{\int dLIPS (BW_a(s) + \kappa e^{i\phi} BW_{a'_1}(s)) (BW_a(s) + \kappa e^{i\phi} BW_{a'_1}(s))^*}, \quad (4)$$

where $A = a'_1$ or $A = a_1$, while $\kappa_{a'_1} = \kappa$ and $\kappa_{a_1} = 1$. For MF-IMR₁, $P(a'_1) = 0.015 \pm 0.002$ while $P(a_1) = 0.935$. For MF-KS₁, $P(a'_1) = 0.041 \pm 0.003$ while $P(a_1) = 1.052$, indicating a large contribution from interference effects.

Multiplying $P(a'_1)$ by the branching ratio for $\tau \rightarrow 3\pi\nu_\tau$, branching ratios for both models of

$$\begin{aligned} BR(\tau \rightarrow a'_1\nu_\tau \rightarrow 3\pi\nu_\tau) &= (1.3 \pm 0.2) \cdot 10^{-3} \quad (MF - IMR), \\ BR(\tau \rightarrow a'_1\nu_\tau \rightarrow 3\pi\nu_\tau) &= (3.6 \pm 0.3) \cdot 10^{-3} \quad (MF - KS) \end{aligned} \quad (5)$$

can be calculated. In the presence of large interference effects, the concept of branching ratio does not have a precise meaning. Nonetheless, the results are of the same order of magnitude as the tentative prediction obtained above, which provides a useful consistency check.

However, other solutions should also be borne in mind. Moderate success, not reported above, has also been obtained in explaining the discrepancy using a different set of results from the VES collaboration [23], who reported the observation of a $J^{PC} = 0^{-+}$ state with an unusually small width, the $\pi(1800)$, which can decay to 3π . Unfortunately, not enough data are available to unambiguously identify the underlying cause.

7 Conclusions

The hadronic structure of the decay $\tau \rightarrow 3\pi\nu_\tau$ has been investigated.

Below $s = 2.3 \text{ GeV}^2$, the 3π invariant mass distribution s is found to be in reasonable agreement with the KS and IMR models. The Dalitz plots and projections are also in broad agreement with the models, showing that the decay proceeds predominantly through a_1 and ρ resonances, although close comparison shows some small discrepancies.

Above $s = 2.3 \text{ GeV}^2$, an enhancement is observed, which is particularly clear in the Dalitz plots and projections. This effect is not described by the models and leads us to hypothesise the existence of a hitherto unobserved decay channel in τ decays consistent with the decay chain $\tau \rightarrow a'_1\nu_\tau$.

The KS model, although having the merit of simplicity and providing a reasonable description of the shape of the s distribution, has three problems. Firstly, the large fitted width of the a_1 leads to a branching ratio prediction at variance with the experimentally measured value. Secondly, the fit to the data at high s values is not particularly good. Thirdly, the distribution over the Dalitz plot at high s differs from the data. One must therefore be cautious of using this model to make measurements which depend strongly on describing the high s region correctly (eg. neutrino mass determinations).

The IMR model gives a fair description of the data, although in the high s region this is in large part due to the polynomial background term. This is clearly a weak point of the model, as it does not provide a physical explanation for the behaviour.

A better description of the data is obtained using the Feindt model to extend the models of KS and IMR by including the effect of the a'_1 . The best description of the data in the high s region is provided by MF-IMR₁ which extends the formalism of IMR by the inclusion of an a'_1 .

The identification of the polynomial background term in the IMR model with an a'_1 resonance is inviting. However, this is not the only possible description of the data. Unfortunately, not enough data are available to unambiguously identify the resonances which may exist in this region. Further theoretical and experimental work is required.

The observation of this effect is interesting for light-meson quark spectroscopy, and may help resolve some of the problems concerning the a_1 meson. It is also important in measuring the spectral functions for τ decay. A good understanding of these is necessary in order to measure the τ neutrino mass. An extra resonance close to the τ mass will distort the population of phase space close to the kinematic limit and, if not correctly accounted for, may lead to erroneous results in the neutrino mass determination.

Acknowledgements

We are greatly indebted to our technical collaborators and to the funding agencies for their support in building and operating the DELPHI detector, and to the members of the CERN-SL Division for the excellent performance of the LEP collider.

References

- [1] PDG96: R.M. Barnett et al., *Phys. Rev.* **D54** (1996) 1.
- [2] J. H. Kühn and A. Santamaria, *Z. Phys.* **C48** (1990) 445.
- [3] N. Isgur, C. Morningstar and C. Reader, *Phys. Rev.* **D39** (1989) 1357.
- [4] M. Feindt, *Z. Phys.* **C48** (1990) 681.
- [5] P.R. Poffenberger, *Z. Phys.* **C71** (1996) 579.
- [6] P. Aarnio et al., DELPHI coll., *Nucl. Instrum. Methods* **A303** (1991) 233.
- [7] P. Abreu et al., DELPHI coll., *Nucl. Instrum. Methods* **A378** (1996) 57.
- [8] P. Abreu et al., DELPHI coll., *Phys. Lett.* **B365** (1996) 448.
- [9] S. Jadach, J. H. Kühn and Z. Was, *Comp. Phys. Comm.* **79** (1994) 503.
- [10] S. Jadach, Z. Was, R. Decker and J. H. Kühn, *Comp. Phys. Comm.* **76** (1993) 361.
- [11] W. Hao et al., 'Study of 3-prong Tau Decays with Kaons', DELPHI 96-76 CONF 8, DELPHI contributed paper pa07-009 to ICHEP'96, Warsaw.
- [12] T. Sjostrand, *Comp. Phys. Comm.* **82** (1994) 74.
- [13] F. A. Berends, P. H. Daverveldt, R. Kleiss, *Comp. Phys. Comm.* **40** (1986) 271.
- [14] R. Akers et al., OPAL coll., *Z. Phys.* **C67** (1995) 45;
K. Ackerstaff et al., OPAL coll., *Z. Phys.* **C75** (1997) 593.
- [15] H. Albrecht et al., ARGUS coll., *Z. Phys.* **C58** (1993) 61.
- [16] P. Bourdon, TAU94, *Nucl. Phys.* B(Proc. Suppl.) **40** (1995) 203.
- [17] R. Kokoski and N. Isgur, *Phys. Rev.* **D35** (1987) 907.
- [18] D. V. Amelin et al., VES Collaboration, *Phys. Lett.* **B356** (1995) 595.
- [19] J. Iizuka, H. Koibuchi and F. Masuda, *Phys. Rev.* **D39** (1989) 3357.
- [20] J. I. Kapusta and E. V. Shuryak, *Phys. Rev.* **D49** (1994) 4694.
- [21] Yu. P. Gouz et al., *Proc. of the XXVI Int. Conf. on High Energy Physics*, Dallas, (1992) 572.
J. H. Lee et al., *Phys. Lett.* **B323** (1994) 227.
- [22] V. G. Shelkov, TAU96, *Nucl. Phys.* B(Proc. Suppl.) **55C** (1997) 195.
- [23] E. B. Berdnikov et al., *Yadernaya Fizika* **57** (1994) 1610;
A. M. Zaitsev, *Yadernaya Fizika* **59** (1996) 1674.

Channel	All s	s ranges (GeV ²)					
		[0.8, 1.1]	[1.1, 1.4]	[1.4, 1.7]	[1.7, 2.0]	[2.0, 2.3]	[2.3, 3.2]
$\tau \rightarrow 3\pi\nu_\tau$	5904.0 ± 35.3	1240.3	1952.3	1405.3	739.1	315.6	152.9
$\tau \rightarrow 3\pi\pi^0\nu_\tau$	778.2 ± 12.8	226.3	188.5	108.0	40.4	9.7	1.2
$\tau \rightarrow 3\pi 2\pi^0\nu_\tau$	31.2 ± 2.9	11.3	4.4	1.4	0.0	0.0	0.0
$\tau \rightarrow K 2\pi\nu_\tau$	297.2 ± 7.9	41.4	93.6	108.1	38.8	3.4	0.7
$\tau \rightarrow 2K\pi\nu_\tau$	75.3 ± 4.6	30.3	17.3	8.1	3.7	0.0	0.0
$\tau \rightarrow other$	48.0 ± 3.1	11.6	6.1	5.0	1.4	1.7	1.1
$Z \rightarrow q\bar{q}$	40.3 ± 6.3	3.9	1.3	2.6	3.9	2.6	5.2
$Z \rightarrow lll$	5.8 ± 1.2	0.0	0.0	0.0	0.0	0.0	0.4

Table 1: Sample composition averaged over the full s range, and in various subranges, estimated from the simulation.

	KS	IMR with polynomial	IMR without polynomial
Mass (MeV)	$1255 \pm 7 \pm 6$	$1207 \pm 5 \pm 8$	1217 ± 7
Width (MeV)	$587 \pm 27 \pm 21$	$478 \pm 3 \pm 15$	475 ± 3

	MF-KS ₀	MF-IMR ₀	MF-KS ₁	MF-IMR ₁
Mass (MeV)	1265 ± 7	1213 ± 5	$1264 \pm 8 \pm 4$	$1196 \pm 4 \pm 5$
Width (MeV)	607 ± 27	476 ± 14	$547 \pm 25 \pm 23$	$425 \pm 14 \pm 8$
κ	0 (fixed)	0 (fixed)	$.75 \pm .06 \pm .02$	$.50 \pm .06 \pm .02$
ϕ (rad)	0 (fixed)	0 (fixed)	$6.1 \pm .2 \pm .0$	$3.2 \pm .2 \pm .0$

Table 2: The fitted a_1 parameters for various models as described in the text. The first error is statistical; the second is due to systematic effects and is presented for the KS and IMR models, as well as for their MF equivalents in which the effect of an a'_1 has been included.

		χ^2 for s distribution						
s -Range (GeV ²)	# bins	KS	IMR with poly- nomial	IMR without poly- nomial	MF-KS ₀	MF-IMR ₀	MF-KS ₁	MF-IMR ₁
[0.5, 2.0]	15	15	19	19	13	22	15	14
[2.0, 3.2]	12	17	17	40	19	42	13	11
[0.5, 3.2]	27	32	36	59	32	64	28	25

		χ^2 for $\sqrt{s_1}$ distributions					
s -Range (GeV ²)	# bins	KS	IMR without poly- nomial	MF-KS ₀	MF-IMR ₀	MF-KS ₁	MF-IMR ₁
[2.3, 3.2]	14	55	57	56	58	21	18
[2.0, 2.3]	14	37	16	42	19	30	16
[1.7, 2.0]	30	68	34	65	36	72	39
[1.4, 1.7]	28	92	48	104	56	129	48
[1.1, 1.4]	28	85	50	105	66	151	59
[0.8, 1.1]	23	38	44	49	46	64	46

		χ^2 for $\sqrt{s_2}$ distributions					
s -Range (GeV ²)	# bins	KS	IMR without poly- nomial	MF-KS ₀	MF-IMR ₀	MF-KS ₁	MF-IMR ₁
[2.3, 3.2]	16	25	46	37	49	13	17
[2.0, 2.3]	15	36	14	56	15	14	17
[1.7, 2.0]	33	43	39	67	34	53	52
[1.4, 1.7]	30	38	36	61	36	57	38
[1.1, 1.4]	27	36	33	40	32	51	30
[0.8, 1.1]	24	32	37	32	36	37	35

Table 3: The agreement between the data and the various model predictions. The upper table shows the agreement in s . The lower two tables show the agreement in s_1 and s_2 . The fit for MF-KS₁ and MF-IMR₁ was performed for the s distribution and for the s_1 and s_2 distributions corresponding to the two highest s -bins. The other fits were made to the s distribution only. The χ^2 values were calculated after the fits, which used a maximum likelihood method. For bins with small numbers of events, an equivalent χ^2 contribution was computed using Poisson probabilities.

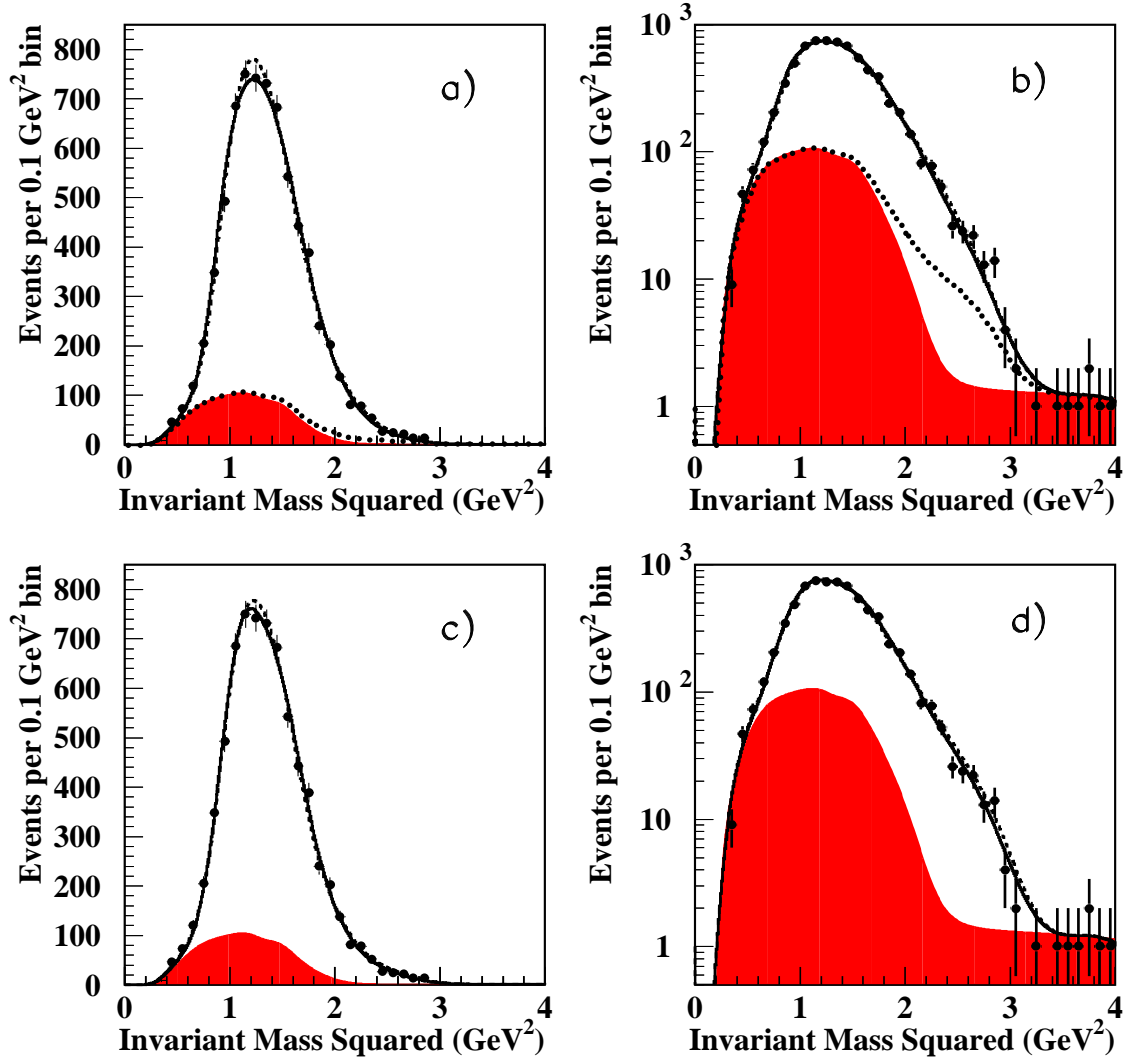


Figure 1: Distribution of 3π invariant mass squared with various models superimposed. The model predictions include the effects of resolution, efficiency and background. The *points* are the data values; the *shaded area* is the estimated background contribution. In plot **a)** the *dashed curve* is the fit to **KS**; the *solid curve* is the fit to **IMR**; the *dotted curve* indicates the contribution of the polynomial background. Plot **b)** is as for a) but on a log scale. In plot **c)** the *dashed curve* is the fit described as **MF-KS₁** in the text; the *solid curve* is that described as **MF-IMR₁**. Plot **d)** is as for c) but on a log scale.

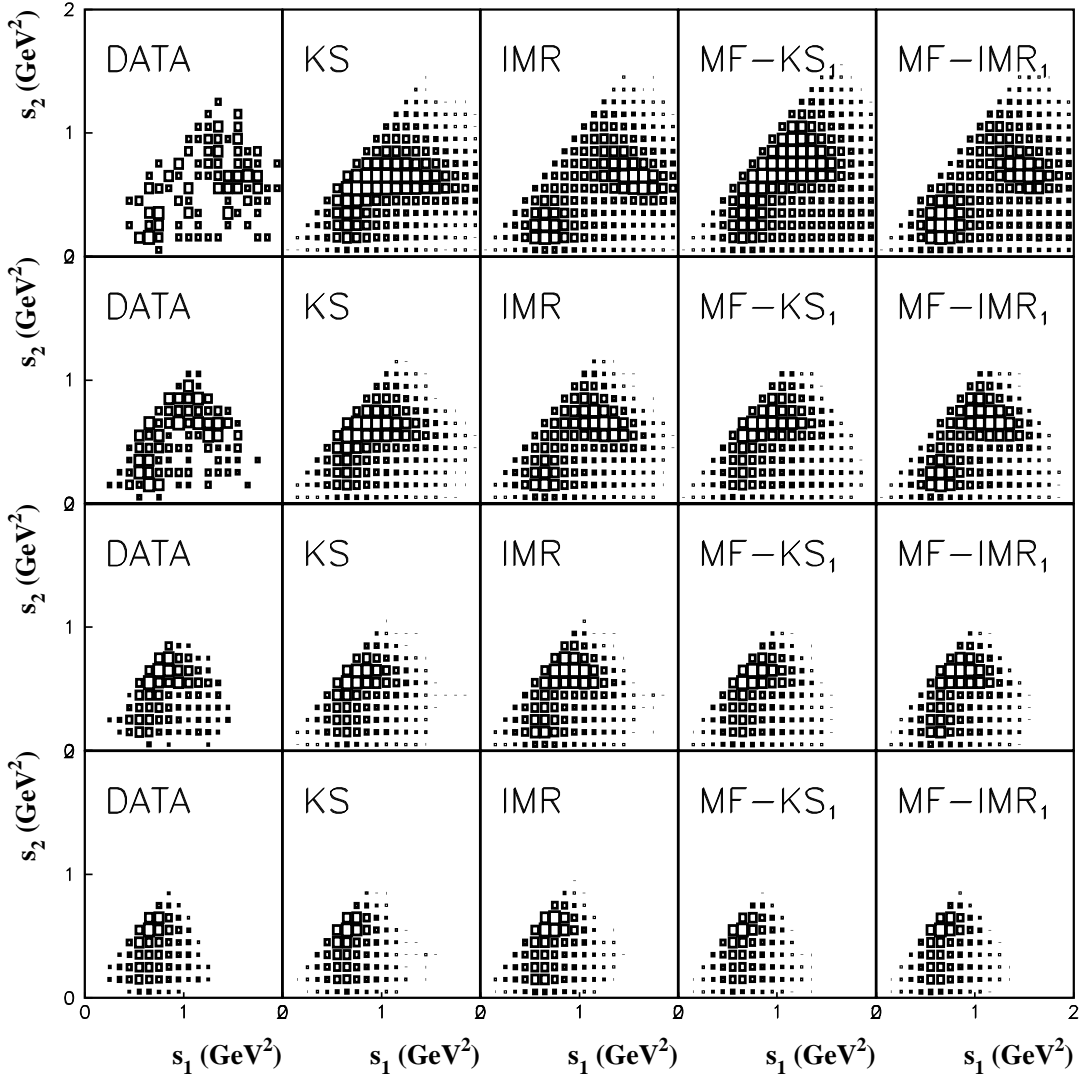


Figure 2: Dalitz plots in sequential s ranges, for the data and the models described in the text. From top to bottom the s ranges (in units of GeV^2) are: $2.3 < s < 3.2$; $2.0 < s < 2.3$; $1.7 < s < 2.0$; $1.4 < s < 1.7$. The model predictions include the effects of detector inefficiencies and resolution but not the backgrounds (see Table 1).

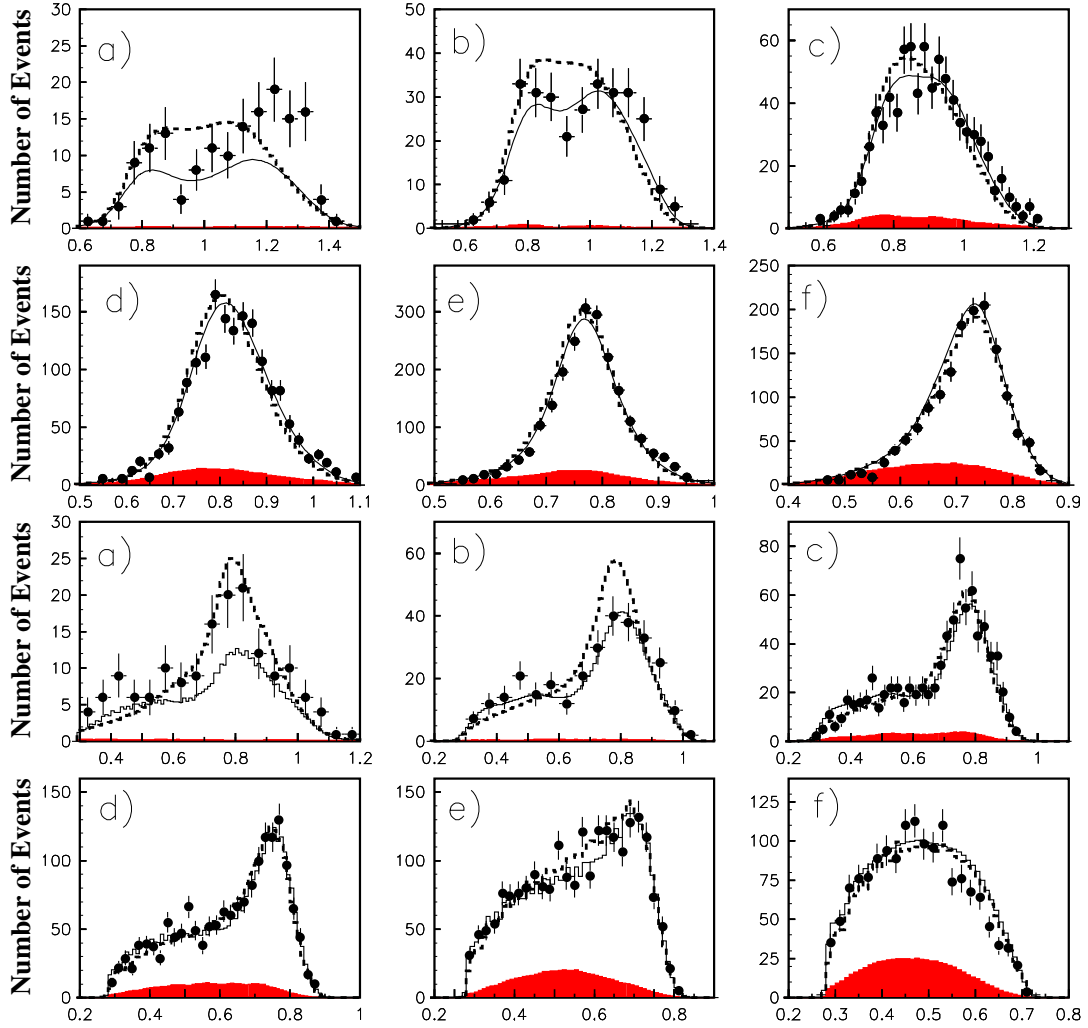


Figure 3: Distributions for $\sqrt{s_1}$ and $\sqrt{s_2}$ for various s bins. The top six plots are for $\sqrt{s_1}$; the bottom six are for $\sqrt{s_2}$. The six s regions (in units of GeV^2) are: a) $2.3 < s < 3.2$; b) $2.0 < s < 2.3$; c) $1.7 < s < 2.0$; d) $1.4 < s < 1.7$; e) $1.1 < s < 1.4$; f) $0.8 < s < 1.1$. The *points* represent the data; the *dotted line* is the **KS** fit; the *solid line* is the resonant part of the **IMR** fit; the *shaded histogram* is the background. The model predictions include the effects of efficiency, resolution and background. Units on the horizontal axis are in GeV.

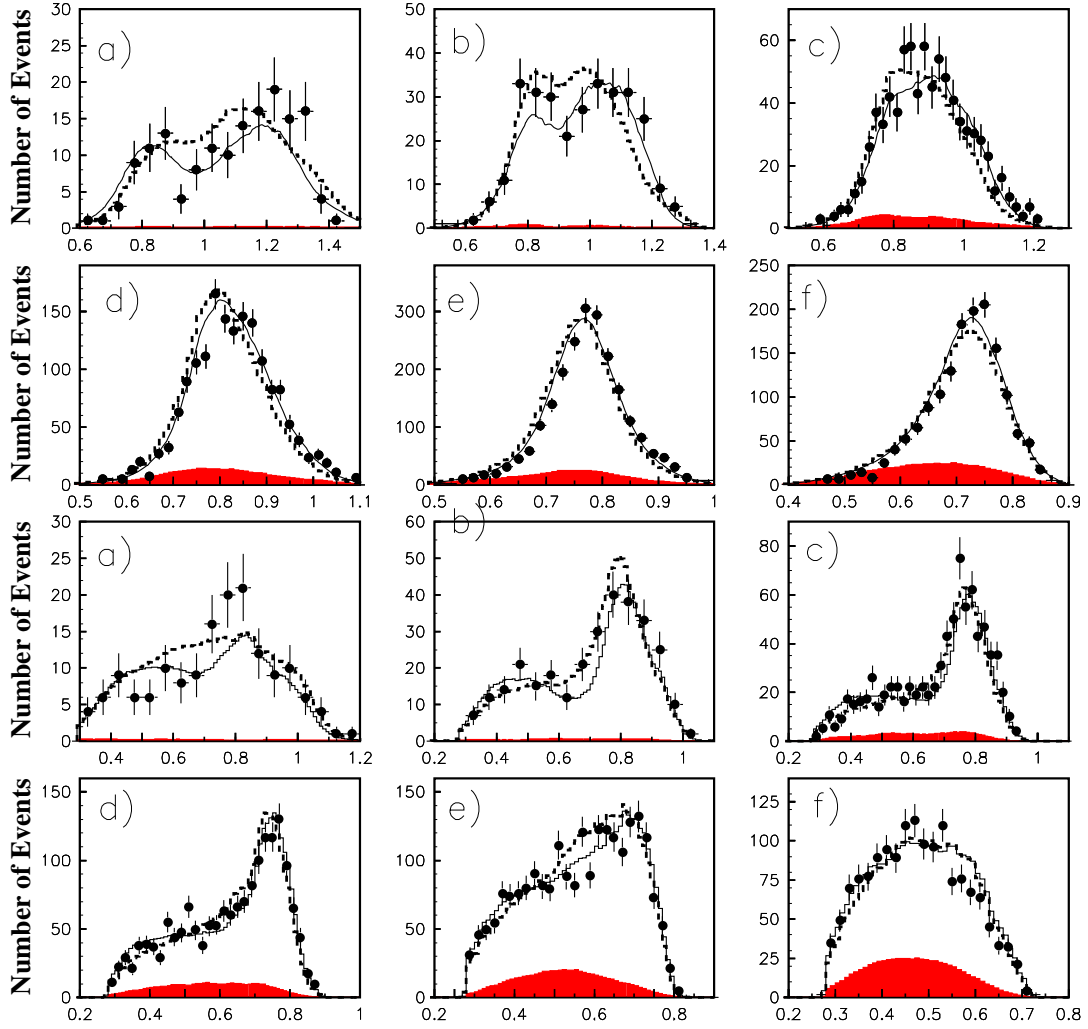


Figure 4: Distributions for $\sqrt{s_1}$ and $\sqrt{s_2}$ for various s bins. The top six plots are for $\sqrt{s_1}$; the bottom six are for $\sqrt{s_2}$. The six s regions (in units of GeV^2) are: a) $2.3 < s < 3.2$; b) $2.0 < s < 2.3$; c) $1.7 < s < 2.0$; d) $1.4 < s < 1.7$; e) $1.1 < s < 1.4$; f) $0.8 < s < 1.1$. The *points* represent the data; the *dotted line* is the fit labelled **MF-KS₁** in the text; the *solid line* is the fit labelled **MF-IMR₁**; the *shaded histogram* is the background from other decay processes. The model predictions include the effects of efficiency, resolution and background. Units on the horizontal axis are in GeV.